

Temperature and flame structure imaging in kerosene swirl-stabilized spray flames at low air flow using TLAF and OH-PLIF

Shirong Xin^a, Yong He^{a,*}, Tao Liu^b, Yingchun Wu^a, Xuecheng Wu^a, Zhihua Wang^a

^a State Key Laboratory of Clean Energy Utilization, Zhejiang University, Hangzhou, 310027, PR China

^b Aero Engine Corp China, Beijing, 100089, PR China

ARTICLE INFO

Handling Editor: Dr. Paul Williams

Keywords:

NTLAF
OH-PLIF
Low air inlet flow rate
Combustion deterioration
Swirling spray combustion

ABSTRACT

Air flowrate is an important parameter for airbrast nozzles and low air inlet flow rate in airbrast type combustors will lead to worse atomization, combustion instability, and increased pollutant emissions. Using non-linear excitation regime two-line atomic fluorescence (NTLAF) thermography imaging and planar laser-induced fluorescence of hydroxyl radical (OH-PLIF), temperature and flame structure in the near-nozzle area are investigated at different low air flow rate to study the combustion deterioration of kerosene swirl-stabilized spray flames. In this concerned area, combustion occurs mainly at the near-wall region but a few OH signals are present at the centerline region except for the kerosene LIF particles. With the air supply getting low, the near-wall OH signals get low, corresponding to the change of indium Stokes and anti-Stokes fluorescence. The temperature in the centerline region is presented to be reduced and the region for the temperature threshold filter expands, indicating the reduction of the downstream hot combustion products brought back by weak swirl, which is closely related to the extremely low air flowrate. Under extremely low air flow rate, the highly fluctuating temperature and weak gas-liquid mixed combustion at the centerline area may tend to cause combustion instability or ignition failure.

1. Introduction

Due to the excellent mixing effect between liquid fuel and air, airbrast nozzles are commonly used as atomizers for turbine engines. Airbrast type combustors utilize the relative velocity between airflow and liquid phase for atomization [1–4], and require lower fuel pressure and higher air flow rate to produce a finer spray, which results in good gas-liquid mixing as well as reduction of soot formation [5,6]. However, the engines may operate under some unfavorable operating conditions, such as relight in areas with thin air, or the start-up phase where the air with a low flowrate is supplied to assist the ignition in order not to blow off. At this time, the combustor is under the condition of insufficient oxidizer, and thus combustion deterioration takes place in the combustion chamber.

The atomizing air to liquid fuel mass ratio (ALR) is an important parameter in the study of airbrast nozzles. Previous research has studied the effect of ALR on atomization and combustion by varying air flowrate with a fixed fuel flow rate to vary the ALR [1,7]. Hence the air flow rate is a frequently studied variable. If the air inlet flow rate is low enough, it will lead to worse atomization and combustion instability, resulting in

ignition failure and a sharp increase in pollutant emissions [7]. In addition, the disappearance of the reverse flow zone (RFZ) in the swirl-stabilized flame is directly related to the decrease of inlet gas momentum [8]. This rapid drop may directly affect the near-nozzle temperature distribution, which harms the flame stability. Therefore, the discussion of conditions at low air flow is meaningful for an advanced understanding of the combustion deterioration of kerosene spray flames.

The effect of the airflow was studied experimentally and numerically in several works of literature before. I.A. Ibrahim et al. [7] created a computational model to investigate the effect of air mass flow on the kerosene spray and combustion characteristics. The numerical results showed that the reverse flow zone was shifted away from the combustor swirler with low air mass flow and some localized high-temperature zones arose resulted of fuel-rich combustion. The experimental results of I.A. Ibrahim et al. [9] showed the high temperature regions were shifted downstream away from the burner head and also were shifted inward close to the combustor by decreasing the ALR. In our previous works [10,11], we developed laser-based methods for the real-time 3D measurement of kerosene droplet distribution in the near-nozzle area of

* Corresponding author. State Key Laboratory of Clean Energy Utilization, Zhejiang University, Zheda Road No. 38, Zhejiang, Hangzhou, 310027, PR China.
E-mail address: heyong@zju.edu.cn (Y. He).

<https://doi.org/10.1016/j.joei.2023.101294>

Received 25 January 2023; Received in revised form 26 May 2023; Accepted 30 May 2023

Available online 30 May 2023

1743-9671/© 2023 Energy Institute. Published by Elsevier Ltd. All rights reserved.

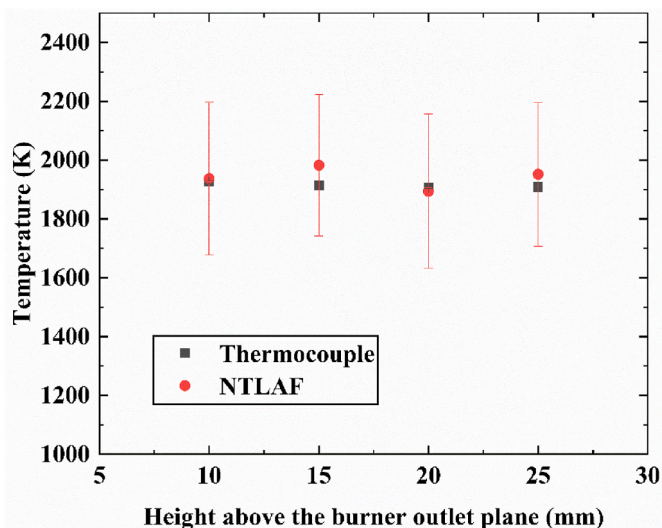


Fig. 3. Results of temperatures at HAB of 10, 15, 20, 25 mm using NTLAF and thermocouple. The absolute error for NTLAF is within 3.7%.

2.2. Experimental setup of optical diagnostics

Fig. 1 shows the optical setup for NTLAF thermography imaging. The LDS821 dye was excited by 532 nm laser from a 10Hz Nd:YAG laser (Powerlite DLS 8010, Continuum) to generate ~ 820 nm laser through a dye laser (Vista, Continuum). After frequency doubling, the needed ~ 410 nm Stokes laser was generated. The ~ 451 nm anti-Stokes laser was produced by tuning the OPO crystal module of the OPO tunable

laser (Radiant 355LD, OPOTEK). Two laser beams were integrated into the same spatial location by a dichroic mirror (DMLP425R, Thorlabs), and passed through a concave lens ($f = -75$ mm) and a convex lens ($f = +500$ mm) to form a planar laser sheet with height of 30 mm and thickness of $250 \mu\text{m}$. Laser energy per pulse and laser sheet profile were confirmed to be an important interference for NTLAF accuracy [21]. In order to monitor the laser fluctuations, before passing through the concave lens, a small part of the combined laser separated by a beam splitter was converged into a small spot by a convex lens and entered a photoelectric detector (PD, DET10 A/M, Thorlabs). Signals of the combined laser received by the PD were recorded through an oscilloscope (WaveRunner 64MXi-A, LeCroy), and the power of each laser pulse can be obtained and monitored in real time after calibration using a laser power meter (S401C, Thorlabs). Moreover, the planar laser sheet passed through a quartz tank and excited the Rhodamine 590 dye in the tank to generate fluorescence. Thus the laser sheet profile could be monitored by detecting the dye fluorescence through a Basler camera. For the NTLAF thermography imaging in kerosene spray flame, the power of the Stokes laser and anti-Stokes laser were both kept at ~ 2.3 mJ/pulse. The time interval between the two laser beams was maintained at 100 ns. The LIF signals were captured by two intensified CCD cameras (PI-MAX 3: 1024i and PI-MAX 4: 512 EM) equipped with 105 mm, $f/4.5$ NIKKOR lenses. The ultra-narrowband filters were proven to be critical for reducing the interference from PAHs and soot [22]. So the signals were spectrally separated with a cubic beam-splitter with $\sim 50\%$ transmission and then were spectrally selected using two customized narrow-band filters (Alluxa) with full widths at half maximum (FWHM) of 1.2 nm (Stokes) and 1.1 nm (anti-Stokes). The in-plane spatial resolution of the matched images was estimated to be $150 \mu\text{m}/\text{pixel}$, and the ICCD gate width was set as 50 ns. Over 200 images were taken by each ICCD camera for NTLAF temperature calculation. Raw images were firstly

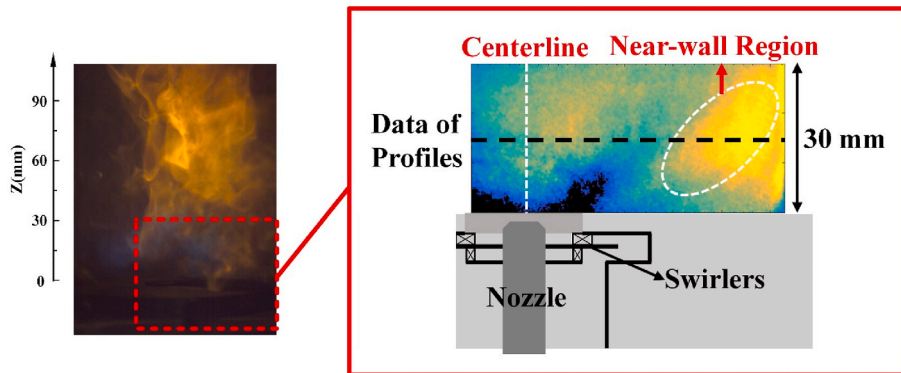


Fig. 4. An real flame image and an annotated image from Case 1, including the locations of centerline (white dashed straight line), near-wall region (white dashed elliptical) and radial profile data (black dashed straight line). Locations of the burner nozzle and the swirlers are also included.

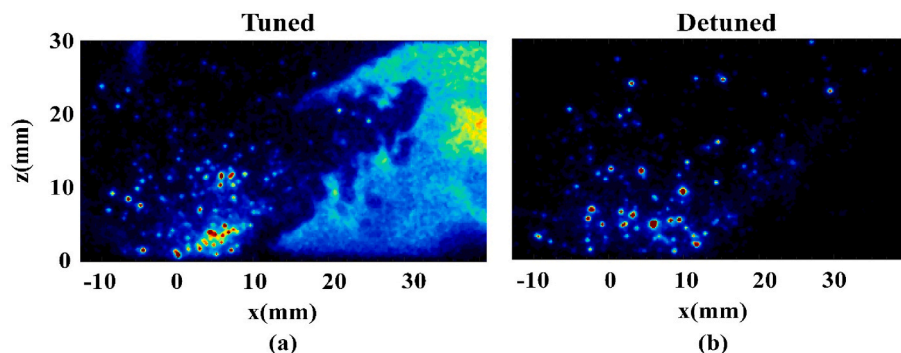


Fig. 5. Instantaneous tuned and detuned OH-PLIF images of Case 1. (a) Tuned process: the laser wavelength is on the OH excitation line to excite OH-PLIF. (b) Detuned process: the laser wavelength is shifted by 0.05 nm to prevent the production of OH-PLIF so that kerosene-LIF can be imaged without OH-LIF.

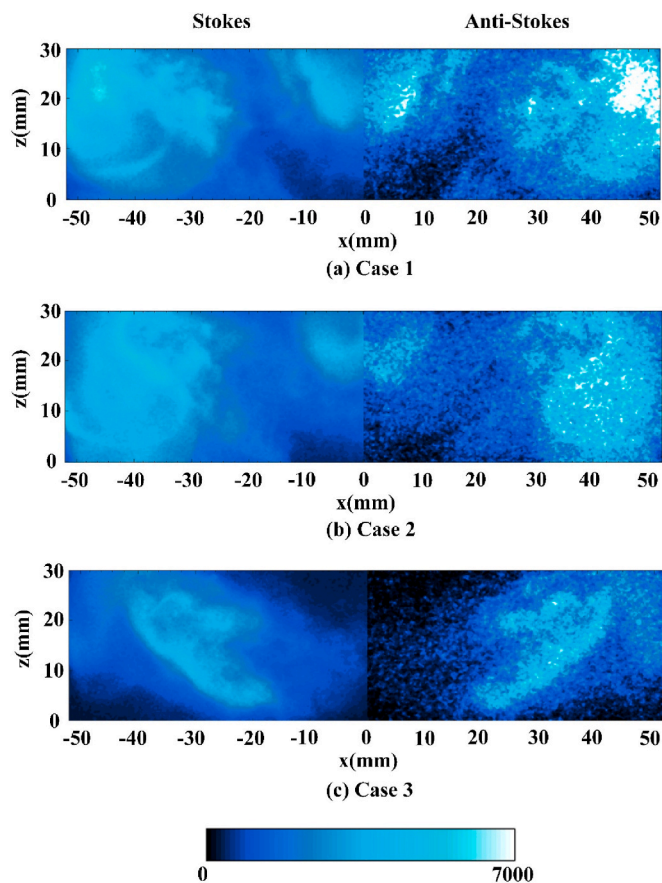


Fig. 6. Instantaneous images of normalized indium fluorescence intensity for different air supply. Stokes and anti-Stokes images are on the left-hand and right-hand side of centerline, respectively (Stokes images have been flipped right-left). Color bar is kept constant in all images. (For interpretation of the references to color in this figure legend, the reader is referred to the Web version of this article.)

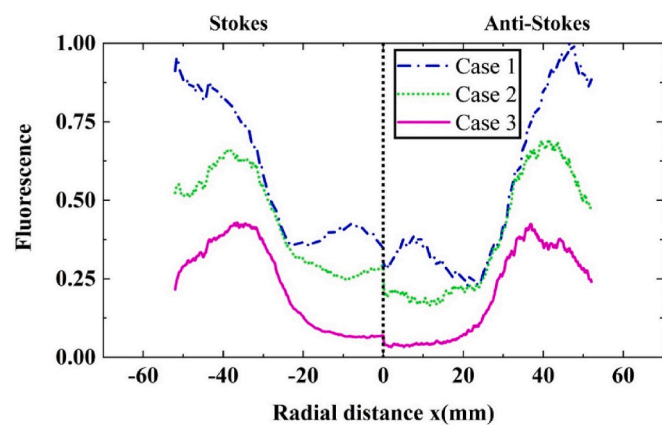


Fig. 7. Mean radial profiles of indium fluorescence measured at $z = 15$ mm, radial profiles of Stokes and anti-Stokes LIF are on the left-hand and right-hand side of centerline.

corrected from spatial energy distribution of the laser sheet, and then were filtered with a two-dimensional 3×3 median filter after size calibration.

The optical arrangement of OH-PLIF was the same as previous study [23]. The energy of the UV laser used for exciting the Q1(5) rotational transition of $A^2\Sigma^+ \leftarrow X^2\Pi(1,0)$ was kept at 10 mJ/pulse. A 310 nm

narrow-band filter (FWHM of 10 nm, peak transmittance of $\sim 60\%$, Alluxa), a 305 nm long-pass filter (305FG01-50, Andover), and a UG11 filter (FGUV11, Thorlabs) were used to eliminate interference of UV laser elastic scattering and acquire clear OH-PLIF images. Image acquisition field of view was the same as NTLAF.

2.3. NTLAF parameters calibration processing

Based on the theory of NTLAF thermography imaging, the temperature T is determined by the strengths of the Stokes and Anti-Stokes signals, F_{21} and F_{20} , through the following equation [16]:

$$T = \frac{\Delta E_{10}/k}{\ln(F_{21} \times (1 + C_S/I_{20})) - \ln(F_{20} \times (1 + C_A/I_{21})) + C_T} \quad (1)$$

where ΔE_{10} is the energy differential between levels of $5^2P_{1/2}$ and $5^2P_{3/2}$ of neutral indium atoms (In) [16], k is the Boltzmann constant, I_{20} and I_{21} are the pulse energy of the Stokes and Anti-Stokes lasers, C_S and C_A were constants that derived experimentally from a plot of fluorescence versus laser pulse energy for the two excitation schemes (Stokes and anti-Stokes). C_T was an experimental system parameter, calibrated by comparing with thermocouple measurement results. C_S , C_A , C_T are determined in a planar premixed laminar flame of a heat flux burner. The burner structure is described in Ref. [24].

For seeding indium to the planar laminar flame, an ultrasonic nebulizer was applied to atomize the InCl_3 solution (2.8 g InCl_3 diluted in 750 mL 95% ethanol) and a certain flowrate of N_2 was used as carry gas. The flowrate of CH_4 , O_2 and N_2 were kept at 1.03 L/min, 1.71 L/min, and 4.55 L/min, respectively. The laminar flame was a fuel-rich flame with stoichiometric ratio of fuel and oxygen of constant 1.22. Fig. 2 shows the one-shot and ensemble-averaged temperature images of the premixed laminar flame of methane. This flame is close to an adiabatic flame and the mean temperatures near the burner center are relatively uniform, approximately 1900K.

The thermocouple calibration should be processed carefully, because C_T significantly affected accuracy of NTLAF. In this work, an experimental method named “assumed zero diameter” was adopted for thermocouple correction. Several B-type thermocouples were used to acquire a plot of temperature versus junction diameter, and the correct temperature can be determined when the junction diameter was extrapolated to 0. The derivation process is detailed in Appendix A. The used thermocouple diameters were 150, 250, 300, 350, 400, 450 μm , respectively.

Fig. 3 shows the results of temperatures at HAB (height above burner) of 10, 15, 20, 25 mm using NTLAF and thermocouple. The flow field and temperature of the hot flue gas will be relatively uniform along the centerline over 5 mm above burner. So the selection of 10, 15, 20 and 25 mm (HAB) for comparison is beneficial to ensure the accuracy of thermocouple measurements without affecting the combustion and flame structure. The absolute error for NTLAF is 69.1 K max, and 10.3 K min, within 3.7%. This indicates that the NTLAF temperature imaging is relatively reliable for engineering measurement. C_T at different HAB are calculated very similar, which are 1.14, 1.20, 1.11, 1.12, respectively.

After calibration, the swirl burner is placed at the same position of heat flux burner, which ensures the calibrated parameters are correct for NTLAF temperature imaging for swirl-stabilized kerosene spray flames.

3. Results and discussion

3.1. Overview of the near-nozzle area

The focus of interest in this work is the near-nozzle area in the kerosene swirling spray flames. This area is subject to large changes in root flame stability and atomization characteristics, so the effect of airflow on temperature is evident in this near-nozzle area and the discussion is practical for the combustion performance. The atomizer of the

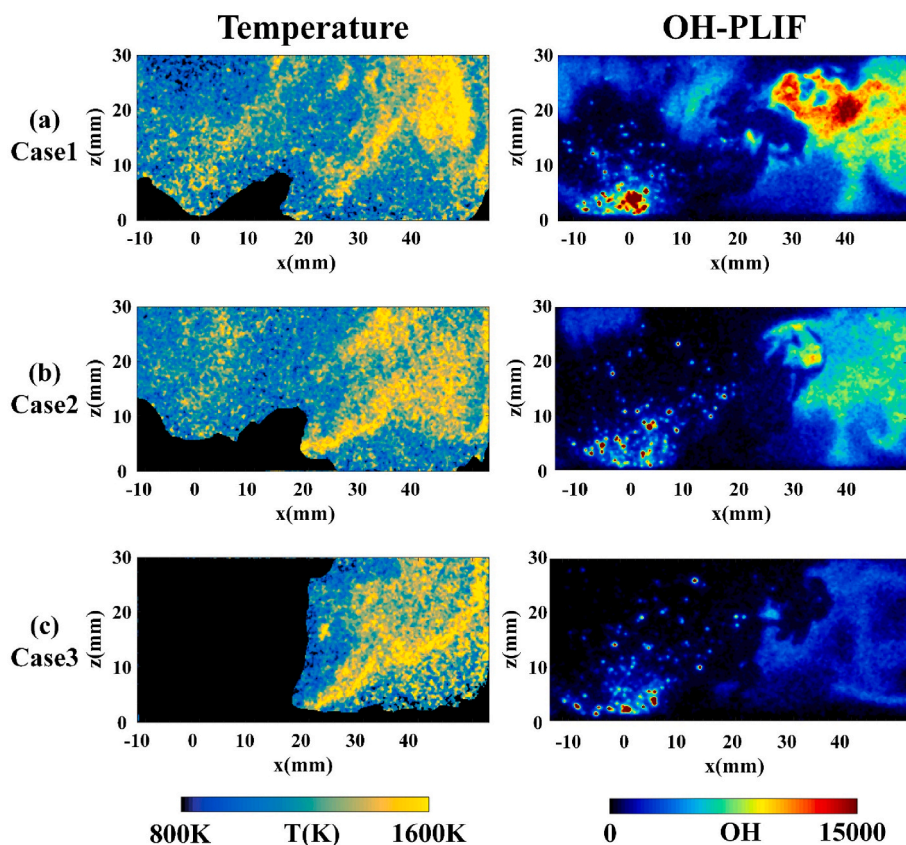


Fig. 8. Instantaneous images of temperature (left-hand side) and OH-PLIF (right-hand side). (a) Case1; (b) Case2; (c) Case3. The particles near the nozzle in the OH-PLIF images are kerosene LIF from droplets that are not completely burned out.

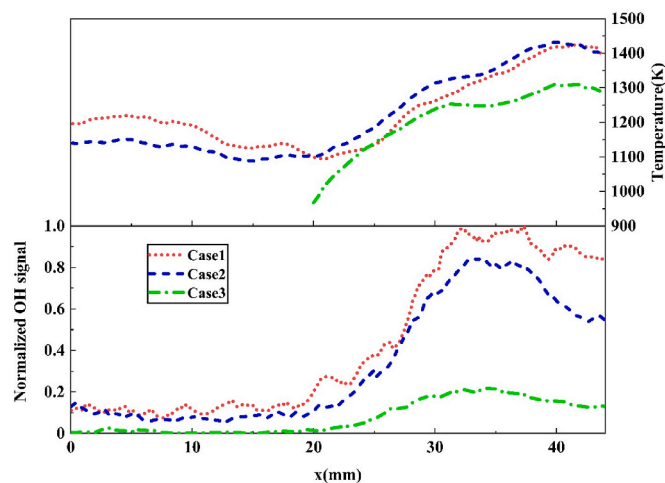


Fig. 9. Radial profiles ($z = 15$ mm) of ensemble-averaged temperature (upside) and ensemble-averaged OH-LIF signal (downside) for Case1 - 3.

burner in this work is a airblast nozzle and the structure of the combustor has been described in detail in Ref. [11]. Fig. 4 shows an image including the burner nozzle and an annotated instantaneous NTLAF temperature image with the locations of centerline, near-wall region and radial profile data. The images of PLIF/NTLAF are 30 mm high above the burner outlet plane.

Instantaneous tuned and detuned images are taken for flame structure visualization and OH-LIF signal validation. As shown in Fig. 5 (a), the OH signals mainly exist in near-wall region. When the UV laser wavelength is shifted by 0.05 nm, the signals disappear, which means

these signals are from OH radicals. In addition, in the tuned or detuned image, most speckled signals at nozzle outlet are from fuel LIF. Because of the density differential, liquid fuel would generate stronger fluorescence than gaseous products under UV laser [25]. To distinguish these speckled signals from OH-LIF, these signals are named “fuel LIF particles”. These fuel LIF particles are recorded although the filters for OH-PLIF have filtered most of the kerosene LIF. Kerosene spray LIF. LIF spectrum of the flame are provided in the Supplemental materials, which will contribute to further understanding of the kerosene LIF particles. Importantly, by comparing the tuned and detuned images, it’s clear that the combustion occurs mostly in the near-wall area and almost never in the centerline of near-nozzle area. The near-wall combustion probably results from the gas-phase mixtures related to the fine mist droplets carried by air. But it seems that the flame is not connected and not in island. This is because the air supply is insufficient, the swirl in the flame is weak, and the liquid kerosene near the nozzle can’t be burned rapidly under the weak reverse flow. But with the swirl developing, the centerline combustion can occur in higher zone of the chamber out of the view of the PLIF image if refer to the real flame image.

3.2. Indium fluorescence of the near-nozzle area

Information of the indium fluorescence signals can help understanding the flow field in the flame and provide some intuitive change of the combustion. Fig. 6 shows instantaneous images of indium fluorescence induced by stokes/anti-stokes lasers. Stokes and anti-Stokes fluorescence in each image are taken simultaneously on either side of the centerline. Color bar is kept constant in all images. In these images, distribution of indium fluorescence presents the well adaptability in spray soot flames, showing relatively high signal-to-noise (SNR). Indium salt is diluted in kerosene fuel and distributes throughout the view under the control of flame flow field. The fluorescence depends on the

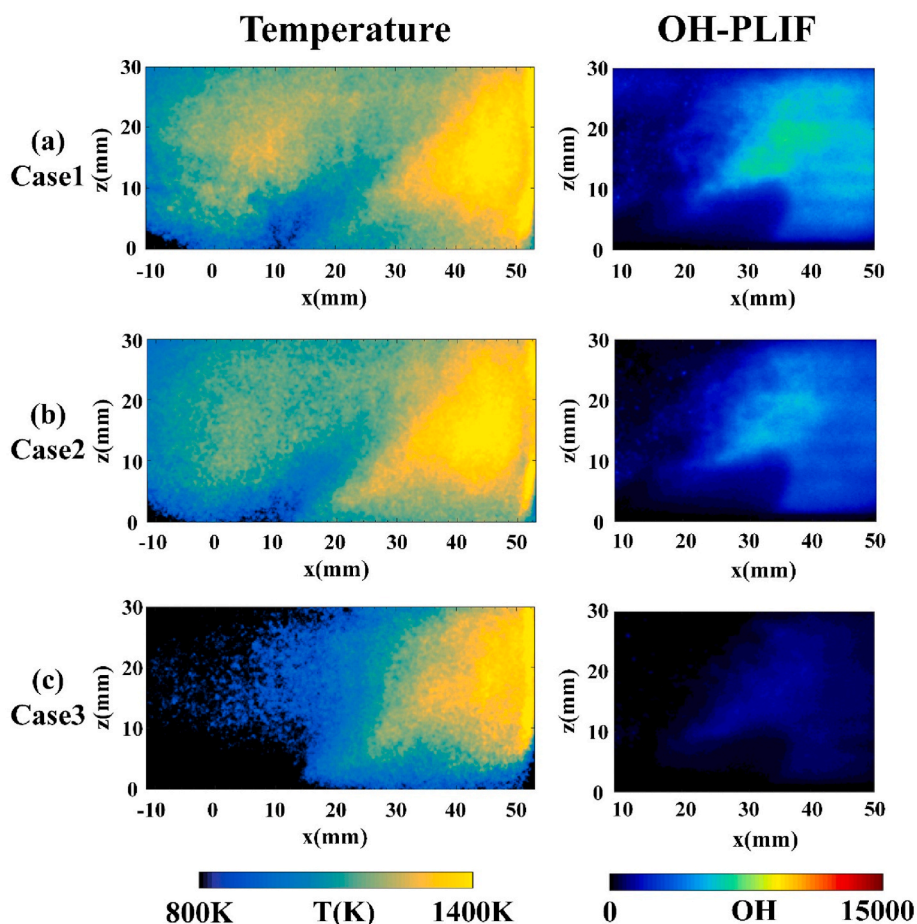


Fig. 10. Images of the ensemble-averaged temperature and OH-LIF signal. Images are 30 mm high above the burner plane. The right edge of the image corresponds to the square quartz chamber wall.

conversion of indium chloride to neutral indium atoms [19,26], and it is commonly accepted that the neutral indium atoms are generated in the redox process of the fuel combustion heat release. Thus the strong signals are typically related to the combustion reaction front. Significantly, unlike the kerosene LIF particles seen in the nozzle outlet of the tuned OH-PLIF image, the indium fluorescence is distributed more evenly, which presents no negative interference from laser Mie scattering or kerosene laser induced fluorescence. Although the centerline regions are lack of combustion reaction, neutral indium atoms can be taken back from the further downstream with the weak reverse flow, unless the air momentum is so low that the reverse flow zone disappears.

Fig. 7 shows the mean radial profiles of indium fluorescence measured at $z = 15$ mm. The Stokes and anti-Stokes fluorescence are normalized to compare at different air flow rate. Over 100 images shot in the succession of indium fluorescence are used for the calculation of the mean radial profiles. The indium fluorescence shows two obvious regions of the centerline region and near-wall region as described in Section 3.1. As shown in Fig. 7, the near-wall fluorescence peaks at $x = \pm 40$ mm are strong, while the signals at the centerline region are relatively weak despite the maximum indium chloride concentration at this region, which means that the generation of neutral indium atoms relies on the interaction with the flame front [27]. Importantly, the signals at the centerline region are closely related to the airflow. When the airflow gets weak, the flow momentum of air becomes lower, the swirl effect becomes weaker, and a strong reverse flow zone fails to form, resulting in the reduction of indium atoms brought back to the centerline area. Like case 3, the signals at the centerline region almost disappear. But as long as the air supply increases to the condition of Case 1, the indium fluorescence at the centerline presents an apparent rapid

increase, both Stokes and anti-Stokes fluorescence. Besides, despite the appearance of hot products such as indium atoms in the centerline region, the incompletely-evaporative kerosene droplets at the nozzle outlet fail to burn off immediately. This means that when the air flow rate is low, the reverse flow is not enough to maintain a stable flame for a long time.

3.3. Results of temperature and OH radical imaging

Fig. 8 shows the combined instantaneous images of OH-PLIF and temperature. The regions with low temperature and low fluorescence intensity in the NTLAF images are filtered with a Matlab algorithm. Because the low temperatures in these regions are unable to generate enough neutral indium atoms for NTLAF calculation, which would result in low SNR in the temperature images. Hence these regions where temperatures are below 800 K are set as a presumed temperature value of 500 K. As shown in Fig. 8, the instantaneous high-temperature region is mainly distributed in the near-wall region. Instantaneous maximum temperature can exceed 2000 K. Correspondingly, signals of hydroxyl radicals exist mainly at the near-wall region. Since OH radicals come from the combustion front of the hydrocarbon fuel with air [28], this indicates that the relatively strong heat release leads to the high temperature in the near-wall region, which demonstrates that the flame in these zones behaves more like a premixed flame. This high temperature keeps the quartz chamber surface hot all the time, which helps the near-nozzle flame attach to the chamber wall or part of the burner exit plane, and then the flame can propagate along the wall. In the centerline area, the instantaneous temperature of Case 1 and Case 2 can exceed 1000 K, but there is no strong combustion happening except for the

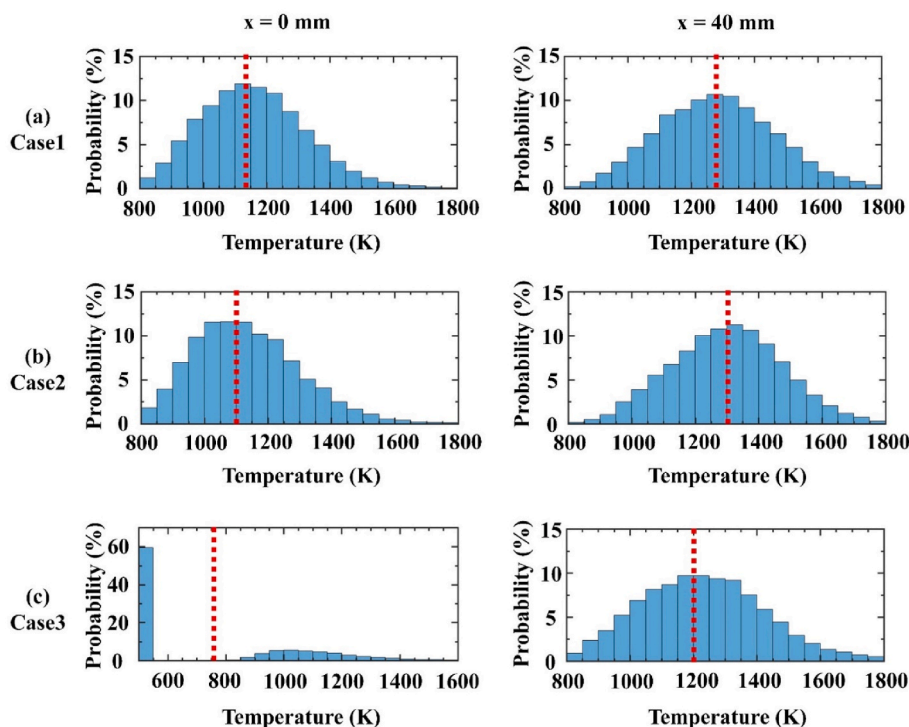


Fig. 11. Temperature histograms for (a) Case1; (b) Case2; (c) Case3 at axial locations of $x = 0$ mm (left-hand side) and $x = 40$ mm (right-hand side). The red vertical dashed line represents the mean temperature for each case at each axial location. (For interpretation of the references to color in this figure legend, the reader is referred to the Web version of this article.)

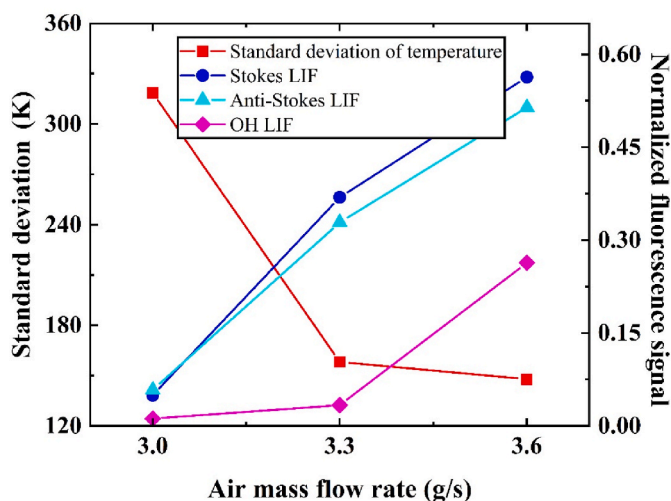


Fig. 12. Point data derived at $z = 25$ mm of the centerline under different air flow rate, consist of temperature standard deviation, Stokes and anti-Stokes LIF intensity of Indium, and LIF intensity of hydroxide radical.

kerosene LIF particles and the weak OH-LIF at the upper end of the field of view. This implies that the temperature here is not influenced greatly by the spray combustion but by the swirl recirculation. In addition, when the air flow rate gets low, the filtered region which is set as a presumed temperature value expands. In the images of Case 3, the filtered region expands throughout the whole centerline region, which indicates that the swirl effect gets considerably worse, leading to unacceptable indium fluorescence intensity for calculation and low temperature across the centerline.

Fig. 9 shows the mean radial profiles of ensemble-averaged temperature and OH-PLIF which are obtained by averaging radial intensities

of 150 instantaneous images. As shown in the figure, the time-averaged OH signals decrease severely with the decrease of air supply due to the reduction of oxidant and worse flow field arrangement. However, in the near-wall region, except an obvious decrease under the condition of case 3, the radial time-averaged temperature distribution of Case 1 and Case 2 shows no significant difference. The anomaly of Case 2 may result from the “bridge region” [14] out of the view of the images, which allows the downstream hot products to flow to the near-wall region and keeps the near-wall temperature from dropping. As for the centerline zone, temperature distinctly decreases with the decrease of air supply. Such as case 3, the centerline region becomes “cold” entirely, mostly close to the NTLAF temperature calculation limit. This means the temperatures in the centerline region are mainly affected by the downstream hot combustion products brought back through the recirculation effect, which are controlled by the weak swirl. Hence the failure of stable ignition in the centerline region probably results in this “cold” temperature. The 2D images of the ensemble-averaged temperature and OH-PLIF can be found in Fig. 10, which provides a visual variation of these two areas.

As shown in Fig. 11, conditional temperature histograms are derived for different cases at the centerline ($x = 0$ mm) and the line close to the near-wall region ($x = 40$ mm). Different from the results of Case 1 and Case 2, when under the condition of Case 3, the mean temperature of these two regions becomes both lower. Additionally, the temperature of 500 K (presumed temperature value) accounts for the majority in the centerline temperature histogram of Case 3, which is consistent with the previous analysis that the temperature in this area is low and almost no neutral indium atoms exist. It's explicit that the swirl effect practically disappears under the condition of case 3. In addition, the mean temperatures are not high (<1400 K) in all these abundant-soot flames because of the imperfect combustion and worse flow field arrangement. But interestingly, the NTLAF shows well adaptability for temperature imaging in these flames. The indium fluorescence can exist below 1200 K in all cases because the soot environment provides a well deficient-oxygen atmosphere for long residence time and easy formation for indium atoms, in spite of the relatively low flame temperature. Thus,

under combustion deterioration such as abundant soot formation, the signal detection limits can be expanded in the range of 800–1200 K for both Stokes and anti-Stokes.

Fig. 12 presents several point data derived at $z = 25$ mm of the centerline for analyzing the characteristics of hot products controlled by the weak swirl. This area is the end of the downstream reverse flow zone, which is the upper edge of the image field of view. It can be found that the decrease of indium atoms with the decrease of air flow rate illustrates the reduction of the reverse-flowing hot products, which leads to the reduced temperature not allowing the kerosene droplets to burn adequately, and OH-LIF thus decreases. This weak gas-liquid mixed combustion at the centerline area is not conducive to the combustion stability. As shown in the figure, the large standard deviation of temperature in the case 3 condition indicates that the temperature is highly fluctuating, which probably means the flameout is prone to happen. This suggests that the instability of combustion or ignition failure tends to occur in the area of gas-liquid mixture at the centerline when the gas flow rate is too low.

4. Conclusions

Utilizing NTLAF and OH-PLIF, the temperature distribution and flame structure of the near-nozzle area are evaluated in the kerosene swirl-stabilized spray flames under different low air flowrate which is the critical parameter for airbrast type combustors. The useful findings from this study are as follows:

1. Flame structure in the near-nozzle area can be defined into near-wall region and centerline region. Combustion occurs mainly at the near-wall region and a few of OH signals present at the centerline region except for the kerosene LIF particles because most near-nozzle fuel can't be burn off immediately with the weak swirl.
2. The near-wall OH signals get low with the air supply gets low, which corresponds to the change of indium atom fluorescence in the near-wall region, both Stokes and anti-Stokes, which relies on interaction

with the flame front. The central indium fluorescence mainly comes from the downstream products, disappearing with the decreased air supply.

3. The temperature in the centerline region is presented to be reduced and the region for temperature threshold filter expands with the decreased air supply, indicating the reduction of the downstream hot combustion products brought back to the nozzle by weak swirl which closely related to the extremely low air flow.
4. Under extremely low air flow rate, the highly fluctuating temperature and weak gas-liquid mixed combustion at the centerline area may tend to cause combustion instability or ignition failure.

CRediT authorship contribution statement

Shirong Xin: Data curation, Formal analysis, Writing - original draft. **Yong He:** Conceptualization, Investigation, Methodology, Validation, Writing - review & editing. **Tao Liu:** Writing - review & editing. **Yingchun Wu:** Writing - review & editing, Resources. **Xuecheng Wu:** Conceptualization, Software, Resources. **Zhihua Wang:** Funding acquisition, Investigation, Writing - review & editing.

Declaration of competing interest

The authors declare that they have no known competing financial interests or personal relationships that could have appeared to influence the work reported in this paper.

Acknowledgments

This work was supported by National Natural Science Foundation of China (52125605) and the Zhejiang Provincial Natural Science Foundation of China (LR23E060001). Authors also thank the support from the Fundamental Research Funds for the Central Universities (2022ZFJH004).

Appendix B. Supplementary data

Supplementary data to this article can be found online at <https://doi.org/10.1016/j.joei.2023.101294>.

Appendix A

“Assumed zero diameter” is an extrapolation method for thermocouple correction. When the fume of the planar laminar flame has a very low Reynolds number (<4) and low outlet velocity (<0.2 m/s), the Nusselt number of the thermocouple junction can be described as:

$$Nu = hd / \lambda = f(Re, Pr) \quad (\text{A.1})$$

$$\lambda / h = d / f(Re, Pr) \quad (\text{A.2})$$

where h is the coefficient of convective heat transfer, λ is the coefficient of heat conductivity, Re and Pr are the Reynolds number and Prandtl number, d is the junction diameter. In the equation above, when $d/f(Re, Pr)$ is infinitely close to 0, $\lambda/h \approx 0$, signifying h is close to infinity and the convective heat transfer of the thermocouple junction far exceeds the thermal radiation or the heat conduction. Considering the convective heat transfer formula $q = h(t_w - t_f)$, the fume temperature t_f is almost equal to the thermocouple junction temperature t_w . Hence, several thermocouples with different diameter can be used to acquire the proportional relation of $d/f(Re, Pr)$ and d .

As shown in Fig. A.1, the used B-type thermocouple diameters are 150, 250, 300, 350, 400, 450 μm , respectively. When the assumed zero diameter d_0 is deduced to be -0.387 mm, $d/f(Re, Pr) = 0$ can be satisfied. According to a plot of temperature versus junction diameter, the actual temperature can be determined by d_0 . One example shown in Fig. A1 indicates that the actual temperature at height above the heat flux burner (HAB) outlet plane of 25 mm can be deduced to be 1908.609 K.

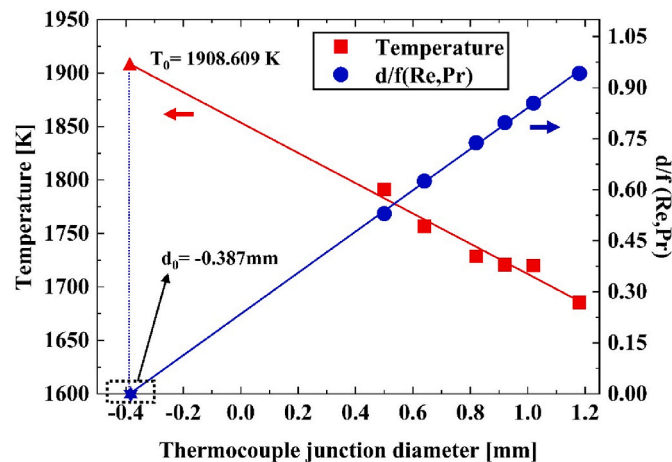


Fig. A.1. Process for deducing the assumed zero diameter d_0 which satisfies $d/f(Re, Pr) = 0$. Blue line, the proportional relation of $d/f(Re, Pr)$ and d ; Red line, the relation of temperature versus junction diameter.

References

- [1] H.M. Gad, I.A. Ibrahim, M.E. Abdel-baky, A.K. Abd El-samed, T.M. Farag, Experimental study of diesel fuel atomization performance of air blast atomizer, *Exp. Therm. Fluid Sci.* 99 (2018) 211–218.
- [2] P. Watanawanyoo, H. Hirahara, H. Mochida, T. Furukawa, M. Nakamura, S. Chaitap, Experimental investigations on spray characteristics in twin-fluid atomizer, *Procedia Eng.* 24 (2011) 866–872.
- [3] A. Basak, J. Patra, R. Ganguly, A. Datta, Effect of transesterification of vegetable oil on liquid flow number and spray cone angle for pressure and twin fluid atomizers, *Fuel* 112 (2013) 347–354.
- [4] R. Ma, B. Dong, Z. Yu, T. Zhang, Y. Wang, W. Li, An experimental study on the spray characteristics of the air-blast atomizer, *Appl. Therm. Eng.* 88 (2015) 149–156.
- [5] M. Guo, N. Shimasaki, K. Nishida, Y. Ogata, Y. Wada, Experimental study on fuel spray characteristics under atmospheric and pressurized cross-flow conditions, *Fuel* 184 (2016) 846–855.
- [6] B. Déjean, P. Berthoumieu, P. Gajan, Experimental study on the influence of liquid and air boundary conditions on a planar air-blasted liquid sheet, Part I: liquid and air thicknesses, *Int. J. Multiphas. Flow* 79 (2016) 202–213.
- [7] I.A. Ibrahim, A.M. Elzallat, M.M. Elsakka, T.M. Farag, H.M. Gad, Numerical study of kerosene spray and combustion characteristics using an air-blast atomizer, *Energy Rep.* 8 (2022) 5974–5986.
- [8] A.M. Elbaz, W.L. Roberts, Stability and structure of inverse swirl diffusion flames with weak to strong swirl, *Exp. Therm. Fluid Sci.* 112 (2020), 109989.
- [9] I.A. Ibrahim, T.M. Farag, M.E. Abdel-baky, A.K. Abd El-samed, H.M. Gad, Experimental study of spray combustion characteristics of air-blast atomizer, *Energy Rep.* 6 (2020) 209–215.
- [10] L. Wang, T. Li, Y. Zhao, H. Zhang, Y. Wu, G. Song, et al., 65 kHz picosecond digital off-axis holographic imaging of 3D droplet trajectory in a kerosene swirl spray flame, *Opt Laser. Eng.* 160 (2023), 107236.
- [11] Y. Wu, L. Wang, W. Lin, G. Song, Y. He, X. Wu, et al., Picosecond pulsed digital off-axis holography for near-nozzle droplet size and 3D distribution measurement of a swirl kerosene spray, *Fuel* 283 (2021), 119124.
- [12] P. Malbois, E. Salaün, B. Rossow, G. Cabot, L. Bouheraoua, S. Richard, et al., Quantitative measurements of fuel distribution and flame structure in a lean-premixed aero-engine injection system by kerosene/OH-PLIF measurements under high-pressure conditions, *Proc. Combust. Inst.* 37 (4) (2019) 5215–5222.
- [13] E. Salaün, F. Frindt, G. Cabot, B. Renou, S. Richard, M. Cazalens, et al., Experimental investigation on NO pollutant formation in high-pressure swirl-stabilized kerosene/air flames using NO-, OH- and kerosene-PLIF and PIV laser diagnostics, in: *Turbomachinery Technical Conference and Exposition, ASME Turbo Expo*, 2020, 2020.
- [14] M.J. Evans, J.A.M. Sidey, J. Ye, P.R. Medwell, B.B. Dally, E. Mastorakos, Temperature and reaction zone imaging in turbulent swirling dual-fuel flames, *Proc. Combust. Inst.* 37 (2) (2019) 2159–2166.
- [15] M. Orain, P. Baranger, C. Ledier, J. Apeloig, F. Grisch, Fluorescence spectroscopy of kerosene vapour at high temperatures and pressures: potential for gas turbines measurements, *Appl. Phys. B* 116 (3) (2014) 729–745.
- [16] P.R. Medwell, Q.N. Chan, P.A. Kalt, Z.T. Alwahabi, B.B. Dally, G.J. Nathan, Development of temperature imaging using two-line atomic fluorescence, *Appl. Opt.* 48 (6) (2009) 1237–1248.
- [17] P.R. Medwell, Q.N. Chan, P.A.M. Kalt, Z.T. Alwahabi, B.B. Dally, G.J. Nathan, Instantaneous temperature imaging of diffusion flames using two-line atomic fluorescence, *Appl. Spectrosc.* 64 (2) (2010) 173–176.
- [18] S.M. Mahmoud, G.J. Nathan, P.R. Medwell, B.B. Dally, Z.T. Alwahabi, Simultaneous planar measurements of temperature and soot volume fraction in a turbulent non-premixed jet flame, *Proc. Combust. Inst.* 35 (2) (2015) 1931–1938.
- [19] P.R. Medwell, Q.N. Chan, B.B. Dally, S. Mahmoud, Z.T. Alwahabi, G.J. Nathan, Temperature measurements in turbulent non-premixed flames by two-line atomic fluorescence, *Proc. Combust. Inst.* 34 (2013) 3619–3627.
- [20] A. Manteghi, Y. Shoshin, N.J. Dam, L.P.H. de Goeij, Two-line atomic fluorescence thermometry in the saturation regime, *Appl. Phys. B Laser Opt.* 118 (2) (2015) 281–293.
- [21] Z. Sun, Z. Alwahabi, B. Dally, G. Nathan, Simultaneously calibrated two-line atomic fluorescence for high-precision temperature imaging in sooting flames, *Proc. Combust. Inst.* 37 (2) (2019) 1417–1425.
- [22] D. Gu, Z. Sun, G.J. Nathan, P.R. Medwell, Z.T. Alwahabi, B.B. Dally, Improvement of precision and accuracy of temperature imaging in sooting flames using two-line atomic fluorescence (TLAF), *Combust. Flame* 167 (2016) 481–493.
- [23] Y. He, Z. Wang, L. Yang, R. Whiddon, Z. Li, J. Zhou, et al., Investigation of laminar flame speeds of typical syngas using laser based Bunsen method and kinetic simulation, *Fuel* 95 (2012) 206–213.
- [24] Z. Wang, S. Wang, R. Whiddon, X. Han, Y. He, K. Cen, Effect of hydrogen addition on laminar burning velocity of CH₄/DME mixtures by heat flux method and kinetic modeling, *Fuel* 232 (2018) 729–742.
- [25] R. Yuan, J. Kariuki, A. Dowlut, R. Balachandran, E. Mastorakos, Reaction zone visualisation in swirling spray n-heptane flames, *Proc. Combust. Inst.* 35 (2) (2015) 1649–1656.
- [26] W. Weng, J. Borggren, B. Li, M. Aldén, Z. Li, A novel multi-jet burner for hot fuel gases of wide range of temperatures and compositions for optical diagnostics of solid fuels gasification/combustion, *Rev. Sci. Instrum.* 88 (4) (2017), 045104.
- [27] P.R. Medwell, A.R. Masri, P.X. Pham, B.B. Dally, G.J. Nathan, Temperature imaging of turbulent dilute spray flames using two-line atomic fluorescence, *Exp. Fluid* 55 (11) (2014) 1840.
- [28] G.P. Smith, J. Luque, C. Park, J.B. Jeffries, D.R. Crosley, Low pressure flame determinations of rate constants for OH(A) and CH(A) chemiluminescence, *Combust. Flame* 131 (1) (2002) 59–69.